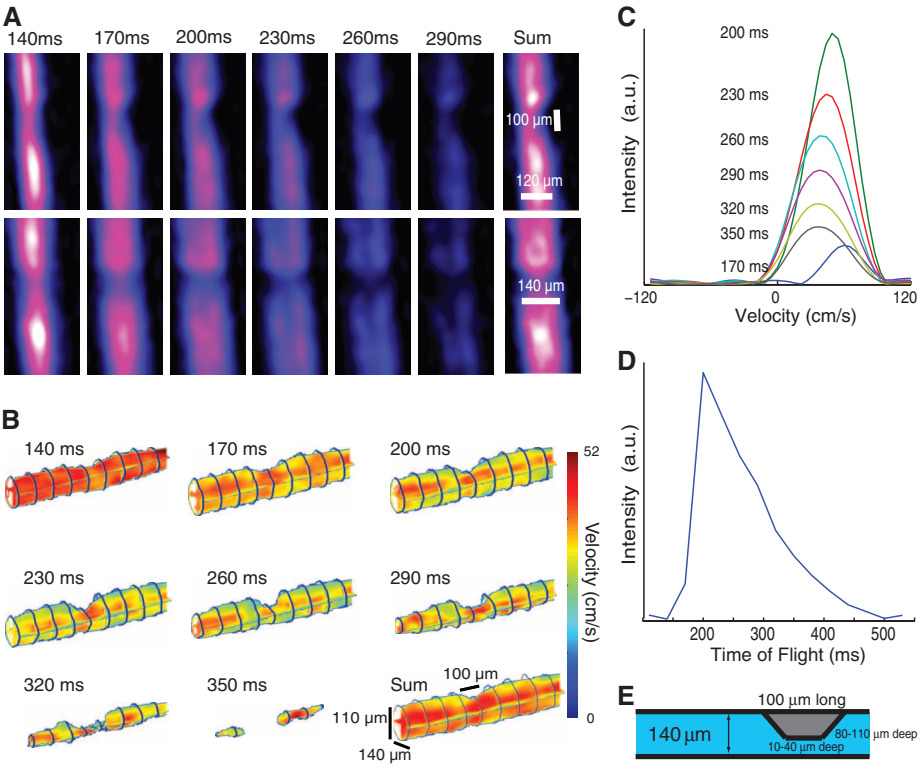

Fig. 3. Accelerating flow in a microfluidic constriction. (**A**) Two-dimensional images (63 × 15 points, *XZ* and *YZ* plane; constriction in *X*) show the high resolution (20 μm) achieved by motion-compensated spatial encoding. The progression reveals fast and slow components of the flow dynamics (see movie S3). The sum is over all TOFs. (**B**) Axial velocity–encoded images [16 (*X*) × 16 (*Y*) × 64 (*Z*)] acquired with 8× subsampling, illustrating acceleration near the constriction and the correlation of velocity and TOF. (**C** and **D**) Around the constriction, flow is dispersive at this spatial resolution; velocity distributions measured at different TOFs (C) reveal fast and slow components, as does the TOF dispersion curve (D). (**E**) Schematic of the constricted microfluidic channel.

References and Notes

1. D. L. Olson, T. L. Peck, A. G. Webb, R. L. Magin, J. V. Sweedler, *Science* **270**, 1967 (1995).
2. Y. Maguire, I. L. Chuang, S. G. Zhang, N. Gershenfeld, *Proc. Natl. Acad. Sci. U.S.A.* **104**, 9198 (2007).
3. C. Massin *et al.*, *J. Magn. Reson.* **164**, 242 (2003).
4. H. Wensink *et al.*, *Lab Chip* **5**, 280 (2005).
5. H. Lee, E. Sun, D. Ham, R. Weissleder, *Nat. Med.* **14**, 869 (2008).
6. Y.-Q. Song, H. Cho, T. Hopper, A. E. Pomerantz, P. Z. Sun, *J. Chem. Phys.* **128**, 052212 (2008).
7. A. J. Moulé *et al.*, *Proc. Natl. Acad. Sci. U.S.A.* **100**, 9122 (2003).
8. J. Jeener, B. H. Meier, P. Bachmann, R. R. Ernst, *J. Chem. Phys.* **71**, 4546 (1979).
9. C. Hilty *et al.*, *Proc. Natl. Acad. Sci. U.S.A.* **102**, 14960 (2005).
10. J. Granwehr *et al.*, *Magn. Reson. Imaging* **25**, 449 (2007).
11. E. Harel, A. Pines, *J. Magn. Reson.* **193**, 199 (2008).
12. E. Fukushima, *Annu. Rev. Fluid Mech.* **31**, 95 (1999).
13. P. T. Callaghan, *Principles of Nuclear Magnetic Resonance Microscopy* (Clarendon, Oxford, 1991).
14. D. G. Cory, A. N. Garroway, *Magn. Reson. Med.* **14**, 435 (1990).
15. M. Lustig, D. Donoho, J. M. Pauly, *Magn. Reson. Med.* **58**, 1182 (2007).
16. D. L. Donoho, *IEEE Trans. Inform. Theory* **52**, 1289 (2006).
17. See supporting material on *Science* Online.
18. J. M. Pope, S. Yao, *Concepts Magn. Reson.* **5**, 281 (1993).
19. G. M. Whitesides, *Nature* **442**, 368 (2006).
20. H. Wu, A. Wheeler, R. N. Zare, *Proc. Natl. Acad. Sci. U.S.A.* **101**, 12809 (2004).
21. C. Monat, P. Domachuk, B. J. Eggleton, *Nat. Photonics* **1**, 106 (2007).
22. S. Koster, E. Verpoorte, *Lab Chip* **7**, 1394 (2007).
23. A. J. deMello, *Nature* **442**, 394 (2006).
24. A. M. Wolters, D. A. Jayawickrama, J. V. Sweedler, *Curr. Opin. Chem. Biol.* **6**, 711 (2002).
25. L. Schröder, T. J. Lowery, C. Hilty, D. E. Wemmer, A. Pines, *Science* **314**, 446 (2006).
26. M. P. Ledbetter *et al.*, *Proc. Natl. Acad. Sci. U.S.A.* **105**, 2286 (2008).
27. J. M. Taylor *et al.*, *Nat. Phys.* **4**, 810 (2008).
28. P. Yager *et al.*, *Nature* **442**, 412 (2006).

29. We thank D. Wemmer for his careful reading of the manuscript and L.-S. Bouchard for helpful discussions. Supported by the U.S. Department of Energy, Office of Basic Energy Sciences, Division of Materials Sciences and Engineering under contract DE-AC02-05CH11231 (V.S.B., J.P., E.H., A.P.). We thank the Agilent Foundation for its generous and unrestricted gift. The Lawrence Berkeley National Laboratory has applied for a patent on aspects of this method. The authors declare no competing interests. **Author contributions:** V.S.B., J.P., E.H., and A.P. designed the experiments. V.S.B., J.P., and E.H. performed the experiments. V.S.B. and J.P. analyzed the data and wrote the paper.

Supporting Online Material

www.sciencemag.org/cgi/content/full/science.1192313/DC1
Materials and Methods
Figs. S1 to S6
Movies S1 to S3
References

14 May 2010; accepted 21 September 2010
Published online 7 October 2010;
10.1126/science.1192313

Probing the Ultimate Limit of Fiber-Optic Strain Sensing

G. Gagliardi,[1]* M. Salza,[1] S. Avino,[1] P. Ferraro,[1] P. De Natale[2]

The measurement of relative displacements and deformations is important in many fields such as structural engineering, aerospace, geophysics, and nanotechnology. Optical-fiber sensors have become key tools for strain measurements, with sensitivity limits ranging between 10^{-9} and $10^{-6}\varepsilon$ hertz $(\mathrm{Hz})^{-1/2}$ (where ε is the fractional length change). We report on strain measurements at the $10^{-13}\varepsilon$-$\mathrm{Hz}^{-1/2}$ level using a fiber Bragg-grating resonator with a diode-laser source that is stabilized against a quartz-disciplined optical frequency comb, thus approaching detection limits set by thermodynamic phase fluctuations in the fiber. This scheme may provide a route to a new generation of strain sensors that is entirely based on fiber-optic systems, which are aimed at measuring fundamental physical quantities; for example, in gyroscopes, accelerometers, and gravity experiments.

Optical sensors and interferometers are widely used for high-sensitivity strain measurements. Gravitational-wave, long-baseline interferometers are the most sensitive strain detectors developed to date, with impressively low detection limits on the order of $10^{-22}\varepsilon$ $\mathrm{Hz}^{-1/2}$ (where ε is the fractional length change), from a few tens of hertz up to the kilohertz range (*1*). However, these detectors are extremely complex and cumbersome, with a length of several kilometers. Smaller–length scale (centimeter) optical-fiber sensors are widespread tools for static and dynamic local-deformation monitoring inside mechanical structures and materials, in environments as diverse as ocean depths, geothermal wells (*2*), and aircrafts (*3*). Strain sensitivities ranging between 10^{-9} and $10^{-6}\varepsilon$ $\mathrm{Hz}^{-1/2}$ are presently feasible with the use of standard telecommunication fiber technology (*4*). Higher strain resolutions have been demonstrated with passive fiber-optic resonators using frequency-stabilized lasers (*5*, *6*)

[1]Consiglio Nazionale delle Ricerche–Istituto Nazionale di Ottica (INO) and European Laboratory for Non-Linear Spectroscopy (LENS), Comprensorio "A. Olivetti," Via Campi Flegrei 34, I-80078 Pozzuoli (Naples), Italy. [2]Consiglio Nazionale delle Ricerche–INO and LENS, Largo E. Fermi 6, I-50125 Firenze, Italy.

*To whom the correspondence should be addressed. E-mail: gianluca.gagliardi@ino.it

achieving $p\varepsilon$ and sub-$p\varepsilon$ levels (1 $p\varepsilon = 10^{-12}\varepsilon$). Most of these approaches are rewarding for strain signals in the acoustic and ultrasonic frequency ranges. On the contrary, for slow-changing phenomena, strain sensing can be very challenging, as it must contend with laser frequency instabilities and drifts that degrade the signal-to-noise ratio. Nonetheless, a sensor capable of tracking very slow deformations with high resolution and accuracy would be of primary importance in several applications, including telescope control (*7*), inertial sensing (*8*), seismic monitoring (*9*), and nanotechnology (*10*). Quasi-static interrogation techniques may have an impact in wavelength-encoded chemical sensing; for instance, with opto-acoustic resonators (*11*) and optical microcavities (*12*). Attempts toward laser noise suppression for fiber sensing that rely on easily available atomic and molecular transitions (*13*, *14*), as well as free-space cavities and interferometers (*5*, *15*), have been made in the past few years. Optical frequency comb (OFC) synthesizers provide an absolute frequency (wavelength) grid with a previously unachieved level of stability from the extreme ultraviolet to the mid-infrared (*16*). OFCs originate from short, mode-locked laser pulses that are equally time-spaced by a radio-frequency clock, and combs are now commercially available in compact fiber-based arrangements (*16*). OFCs have been proposed as light sources for interferometers aimed at accurate distance and displacement determinations (*17*), as they can guarantee the traceability of displacements to an absolute time standard (*18*).

The ultimate performance of most fiber-optic systems is hampered by thermally induced phase noise (*19*). The physical problem is similar to Johnson's noise in electrical circuits, and it can be treated in a way analogous to Nyquist theory by starting from thermal equilibrium energy fluctuations. This is the case for long-fiber interferometers and Sagnac gyroscopes (*20*, *21*). The same noise appears in the low-frequency spectrum of fiber lasers (*22*). This issue has been extensively investigated, both theoretically and experimentally, over the past decades, and different models have been proposed (*23*) but never tested in the infrasonic region (1 mHz to 20 Hz).

We demonstrate strain measurements using a fiber Bragg-grating (FBG) resonator sensor by means of a laser that is stabilized against an OFC. The OFC provides a phase-coherent link between the laser and a radio-frequency oscillator referenced to the primary time standard, leading to an interrogation system that is almost free of laser frequency noise. The response of our sensor is approaching the thermally induced noise limit (*23*). In the experimental setup (Fig. 1), an extended-cavity diode laser emitting ~1560 nm is phase-locked to the nearest comb tooth with a frequency offset given by a 30-MHz local oscillator [further details in (*24*)]. The comb repetition rate and carrier-envelope offset frequency are phase-locked to a 10-MHz oven-controlled quartz oscillator (OCXO) (*24*). We adopted a Pound-Drever-Hall (PDH) scheme to lock the laser to the FBG resonator [reference S3 in (*24*)]. Actually, two secondary carriers (SCs) are created by phase modulation from a tunable synthesizer. A typical PDH signal is thus obtained for the SCs and sent to a servo that drives the synthesizer to frequency-lock one of them to a cavity mode. Hence, active interrogation of the sensor is carried out by the SC, adding only a negligible noise from the synthesizer, whereas the laser carrier remains phase-locked to the OFC. Strain readout is taken from the locking servo signal.

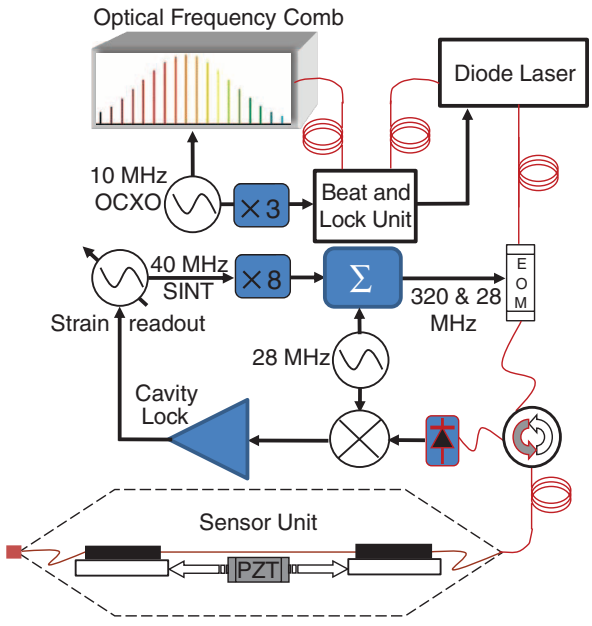

Fig. 1. Experimental setup. The system is composed of a sensor unit, a diode laser, an OFC with a reference oscillator (OCXO), and a laser-comb phase-lock unit. All optical units are connected by optical fibers. The sensing element is a Fabry-Pérot fiber resonator formed by two identical single-mode 99% FBG reflectors, placed at a relative distance L = 130 mm along an acrylic-coated silica fiber. A PZT is used to modulate the cavity length. The resonator is thermally and acoustically shielded from the environment. A seismic insulation in the horizontal and vertical planes, at frequencies above 0.7 Hz, is provided with a latex-cord pendulum suspension. SINT, synthesizer; EOM, electro-optic modulator.

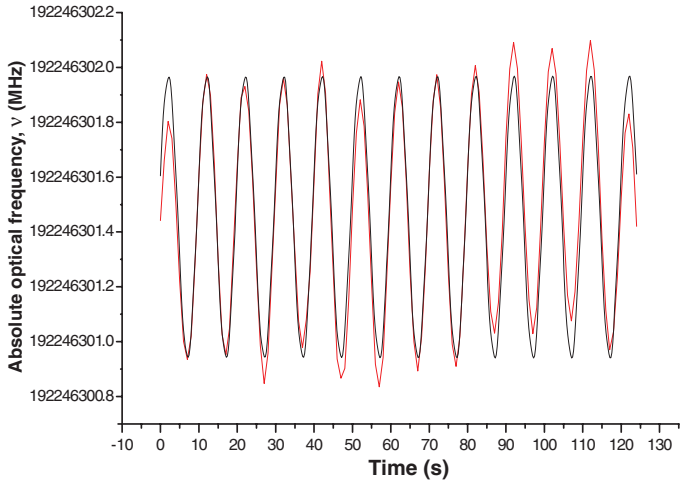

Fig. 2. Direct absolute frequency measurements of the SC frequency are performed by a precision counter (red line) referred to the OCXO when a slow deformation is applied ($2n\varepsilon_{rms}$ at 100 mHz). A sinusoidal fit to the experimental values is also represented (black line).

Mechanical perturbations in the intracavity fiber are seen as proportional changes of the resonance frequency position and translated into SC frequency changes by the locking loop. To estimate the strain resolution, we caused a known deformation in the sensor by applying a voltage to the piezoelectric actuator (PZT). We then carried out a careful calibration of the PZT displacement by using the PDH linear slope as a frequency-to-strain transducer (*25*). Figure 2 shows a measurement performed in the time domain for an excitation of $2n\varepsilon_{rms}$ at 0.1 Hz (1 $ne = 10^{-9}\varepsilon$, and ε_{rms} is the root mean square fractional length change). The data on the vertical axis were obtained by frequency counting the SC shift with a 12-digit precision counter linked to the OCXO and are expressed as absolute optical frequency variations [via eq. 1 in (*24*)]. The time-domain frequency counts are proportional to the slow deformation, as they contain information on frequency changes of the cavity resonance with respect to the OFC, and can be directly back-traced to the OCXO. The laser serves as a secondary length standard that is directly compared to the fiber cavity optical path length during strain measurements. The plot exhibits a clean sinusoidal signal with a weak, superimposed modulation at a lower frequency (~10 mHz), which can be attributed to the torsion-oscillation resonance of the insulation pendulum. A slow change of the center frequency, caused by temperature drifts in the fiber, is barely visible. However, the root mean square value of the oscillation amplitude in Fig. 2 is consistent with that expected from the PZT voltage

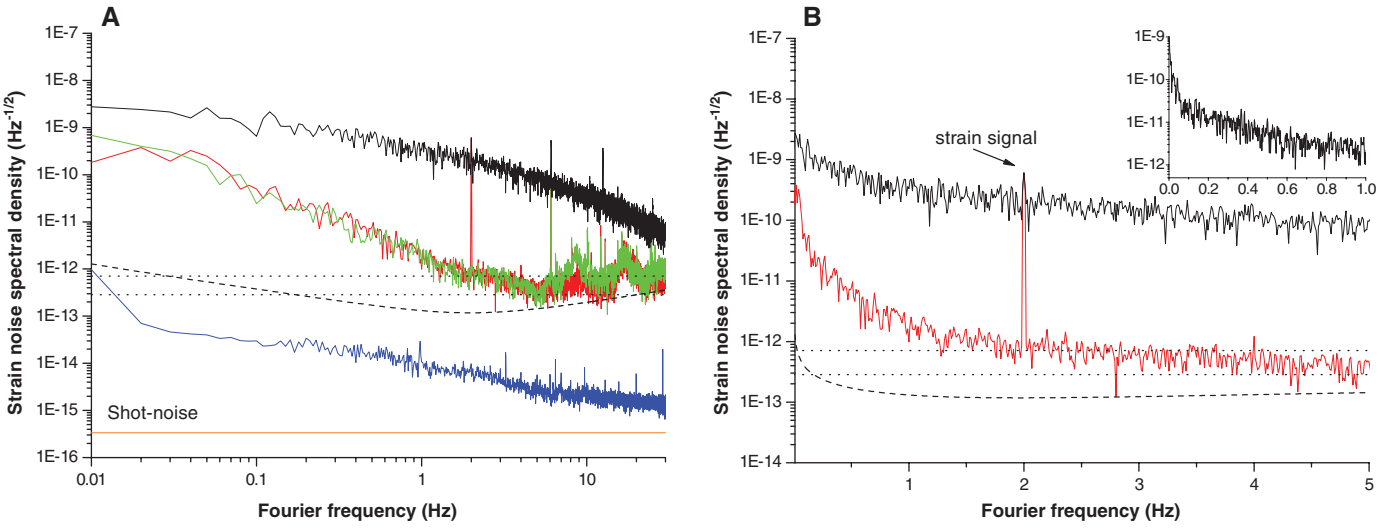

Fig. 3. (**A**) Strain spectrum recorded when the laser is locked to the OFC (red line) and in the free-running condition (black) with a 2-Hz signal for strain calibration. The green trace is recorded when no strain is applied, whereas the dotted lines represent the thermodynamic noise range predicted in (*23*). The blue and orange lines correspond to the measured dark electronic noise and the theoretical shot noise (200-μW power), respectively. The dashed curve represents the strain-noise spectral density derived from the measured OCXO phase noise. (**B**) Same recording as in (A), shown on a magnified horizontal scale to point out the signal enhancement deriving from comb stabilization (55 dB around 1 to 2 Hz). (Inset) A higher-resolution spectrum (acquisition time = 1500 s) shows the strain noise below 1 Hz.

and confirms the correctness of the low-frequency calibration procedure.

Based on the measured response, we applied a sinusoidal displacement of $61p\varepsilon_{rms}$ to the 130-mm intracavity fiber and assessed the strain resolution via a fast Fourier transform of the servo output. The resulting strain-noise spectral density curves in the infrasonic range are shown in Fig. 3A with a superimposed perturbation at 2 Hz for voltage-to-strain conversion. From the average noise floor in Fig. 3B, a lower bound of $550f\varepsilon_{rms}/\sqrt{Hz}$ around 2 Hz can be observed, with a minimum of $350f\varepsilon_{rms}/\sqrt{Hz}$ at 5 Hz (1 fε = 10^{-15}ε). The noise level is still 60 dB higher than the expected shot-noise–limited resolution (*5*) and is 40 dB above the measured electronic background. A recording with a narrower-resolution bandwidth in the low-frequency region is shown in the inset of Fig. 3B, illustrating a detection limit of $20p\varepsilon_{rms}/\sqrt{Hz}$ and $10p\varepsilon_{rms}/\sqrt{Hz}$ at 50 mHz and 200 mHz, respectively. It is worth noting the dramatic improvement resulting from laser frequency stabilization to the OFC, with a 40- to 60-dB enhancement in the frequency range between 0.1 and 10 Hz. In Fig. 3B, the strain-noise contribution from the OFC reference oscillator is also shown. When the laser is locked to the comb, a mere multiplication of the OCXO phase noise up to the optical domain [× N, where N is defined in (*24*)] yields a level of $120f\varepsilon/\sqrt{Hz}$ at 2 Hz. This suggests that the actual resolution, around 1 Hz, is ~15 dB above that predicted from oscillator-induced laser-frequency noise.

We have also experimentally compared the previous strain spectrum with that obtained when the comb is driven by an oscillator that has a phase noise of –80 dB/Hz at 2 Hz; i.e., at least 40 dB above the OCXO level. A degradation of only 20 to 25 dB could be appreciated from the strain-noise spectrum (fig. S1), which confirms that the dominant noise does not originate within the OFC. This implies that the system is still not limited by the locked laser stability. When light is transmitted through the fiber, the medium itself imposes a spectrum of refractive index (phase) fluctuations that affects the minimum detectable strain (*19*). A complete theoretical model for finite-cladding fibers provides the phase-noise spectral density and also contains an analytical expression for the low-frequency behavior (*23*). According to this model, the low-frequency noise spectrum should be nearly flat. Apparently, a reliable estimate of this noise level is seriously affected by the uncertainty of the involved parameters (*22*, *26*), though the correctness of the model has never been tested for frequencies below 250 Hz (*20*, *27*), where thermal effects can be more relevant. Particularly, the insulating boundary conditions of the fiber may influence the thermal response because they reflect on the heat dissipation, as already established for fiber lasers (*22*). In Fig. 3, A and B, two thermal-noise curves are simulated with the use of an effective fiber length $L_{eff} = 2FL/\pi$, with Finesse F = 110 (L is the resonator length). These curves correspond to the extreme cases calculated with the fiber thermo-optic and thermal-expansion coefficients available from the literature (*19*, *22*, *28*). We observe that the data obtained in this investigation exhibit a nonflat spectrum with a plateau of $312 \pm 13f\varepsilon/\sqrt{Hz}$ (from a least-squares fitting of the noise baseline). This value is fully consistent with the predicted thermal-noise range above 1 Hz (Fig. 3). The OCXO phase noise is well below the thermal-induced, refractive-index noise floor from 0.2 to 10 Hz, which thereby represents the real limitation to strain resolution. Therefore, the broad spectral features from 10 to 30 Hz are most likely caused by mechanical coupling of thermodynamic noise to the resonator.

At very low frequencies (below 1 Hz), noise increases slowly with a $1/f$ dependence. Although a seismic noise contribution is likely in low-frequency strain monitoring, it should decay approximately with $1/f^2$ (*29*). Alternatively, this noise roll-up

Fig. 4. Strain spectrum at acoustic frequencies with a calibration signal at 1.5 kHz and thermodynamic noise curves (dotted lines). The three sharp peaks at lower frequencies are due to 50-Hz line voltage coupling to the electronics. The central broad feature can be attributed to acoustic resonances of the laser cavity mount or the OFC.

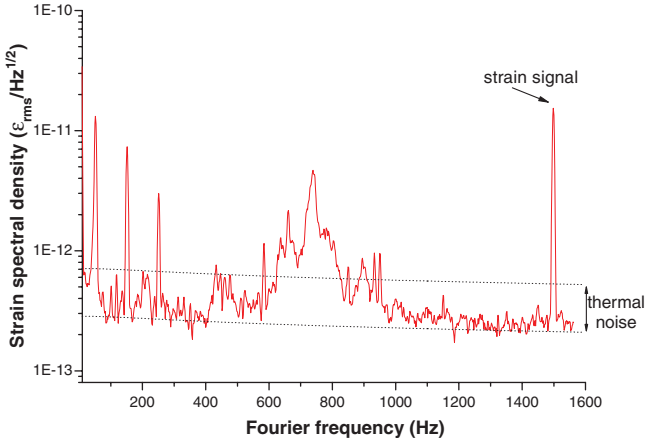

could be attributed to the OCXO phase noise, but the scaling law must be different, as shown by the dashed curve in Fig. 3A. Excess thermally induced fluctuations due to insulating boundary conditions (fiber acrylic buffer) could be responsible for this unexpected response (*22*). Moving toward lower frequencies (inset in Fig. 3B), below 0.1 Hz, a seismic contribution starts to be evident. The noise spectrum recorded from 10 to 1600 Hz (Fig. 4) indicates the resolution in the case of acoustic-strain detection. On these time scales, the laser-emission spectrum is narrowed down to the comb-tooth linewidth by the phase lock (fig. S2). Again, the noise level of this investigation approaches the thermodynamic noise with a minimum of $220f\varepsilon_{rms}/\sqrt{Hz}$ around 1.5 kHz.

At present, the system strain resolution is limited by thermally induced phase fluctuations in the fiber, and this limit has been experimentally identified via the dramatic noise reduction resulting from laser phase-lock to the OFC. A more quantitative understanding of thermally induced phase noise can be performed with the use of fiber-optic cavities with different lengths and materials in well-controlled thermodynamic conditions.

References and Notes

1. D. Reitze, *Nat. Photonics* **2**, 582 (2008).
2. M. Niklès, F. Ravet, *Nat. Photonics* **4**, 431 (2010).
3. M. Jones, *Nat. Photonics* **2**, 153 (2008).
4. Y. J. Rao, *Meas. Sci. Technol.* **8**, 355 (1997).
5. J. H. Chow, D. E. McClelland, M. B. Gray, I. C. M. Littler, *Opt. Lett.* **30**, 1923 (2005).
6. G. Gagliardi, S. De Nicola, P. Ferraro, P. De Natale, *Opt. Express* **15**, 3715 (2007).
7. D. G. MacMynowski, *Appl. Opt.* **48**, 2105 (2009).
8. T. T. Y. Lam, G. Gagliardi, M. Salza, J. H. Chow, P. De Natale, *Meas. Sci. Technol.* **21**, 094010 (2010).
9. G. A. Cranch *et al.*, *IEEE Photon. Technol. Lett.* **15**, 1579 (2003).
10. Y. Bitou, *Precis. Eng.* **33**, 187 (2009).
11. L. Su, S. R. Elliott, *Opt. Lett.* **35**, 1212 (2010).
12. F. Vollmer, S. Arnold, *Nat. Methods* **5**, 591 (2008).
13. A. Arie, B. Lissak, M. Tur, *J. Lightwave Technol.* **17**, 1849 (1999).
14. T. T. Y. Lam *et al.*, *Appl. Opt.* **49**, 4029 (2010).
15. T. T. Y. Lam, J. H. Chow, C. M. Mow-Lowry, D. E. McClelland, I. C. M. Littler, *IEEE Sens. J.* **9**, 983 (2009).
16. P. Maddaloni, P. Cancio, P. De Natale, *Meas. Sci. Technol.* **20**, 052001 (2009).
17. P. Balling, P. Kren, P. Masika, S. A. van den Berg, *Opt. Express* **17**, 9300 (2009).
18. Y. Bitou, *Opt. Lett.* **34**, 1540 (2009).
19. W. H. Glenn, *IEEE J. Quantum Electron.* **25**, 1218 (1989).
20. S. Knudsen, A. B. Tveten, A. Dandridge, *IEEE Photon. Technol. Lett.* **7**, 90 (1995).
21. R. P. Moeller, W. K. Burns, *Opt. Lett.* **21**, 171 (1996).
22. S. Foster, A. Tikhomirov, M. Milnes, *IEEE J. Quantum Electron.* **43**, 378 (2007).
23. K. H. Wanser, *Electron. Lett.* **28**, 53 (1992).
24. Materials and methods are available as supporting material on *Science* Online.
25. J. H. Chow, I. C. M. Littler, G. de Vine, D. E. McClelland, M. B. Gray, *J. Lightwave Technol.* **23**, 1881 (2005).
26. E. Rønnekleiv, *Opt. Fiber Technol.* **7**, 206 (2001).
27. K. H. Wanser, A. D. Kersey, A. Dandridge, *Opt. Photonics News* **4**, 37 (1993).
28. S. Chang *et al.*, *Chin. J. Phys.* **38**, 437 (2000).
29. D. C. Agnew, *Rev. Geophys.* **24**, 579 (1986).

30. We thank M. Prevedelli, A. Arie, M. De Rosa, and J. H. Chow for helpful discussions. Technical assistance on the electronic setup was provided by R. Abbate, who passed away in September 2008. We thank Avanex Corp. (San Donato, Milan, Italy) for kindly providing part of the equipment. This experiment was partly funded by Ente Cassa di Risparmio di Firenze.

Supporting Online Material

www.sciencemag.org/cgi/content/full/science.1195818/DC1
Materials and Methods
Figs. S1 and S2
References

29 July 2010; accepted 19 October 2010
Published online 28 October 2010;
10.1126/science.1195818

Loss of Carbon from the Deep Sea Since the Last Glacial Maximum

Jimin Yu,[1]* Wally S. Broecker,[1] Harry Elderfield,[2] Zhangdong Jin,[3] Jerry McManus,[1] Fei Zhang[3]

Deep-ocean carbonate ion concentrations ($[CO_3^{2-}]$) and carbon isotopic ratios ($\delta^{13}C$) place important constraints on past redistributions of carbon in the ocean-land-atmosphere system and hence provide clues to the causes of atmospheric CO_2 concentration changes. However, existing deep-sea $[CO_3^{2-}]$ reconstructions conflict with one another, complicating paleoceanographic interpretations. Here, we present deep-sea $[CO_3^{2-}]$ for five cores from the three major oceans quantified using benthic foraminiferal boron/calcium ratios since the last glacial period. Combined benthic $\delta^{13}C$ and $[CO_3^{2-}]$ results indicate that deep-sea-released CO_2 during the early deglacial period (17.5 to 14.5 thousand years ago) was preferentially stored in the atmosphere, whereas during the late deglacial period (14 to 10 thousand years ago), besides contributing to the contemporary atmospheric CO_2 rise, a substantial portion of CO_2 released from oceans was absorbed by the terrestrial biosphere.

Past atmospheric CO_2 concentrations recorded in ice cores and deep-ocean $\delta^{13}C$ recorded in benthic foraminiferal carbonates indicate that the amounts of carbon stored in atmosphere and terrestrial biosphere during the Last Glacial Maximum (LGM) [24 to 18 thousand years ago (ka)] were considerably smaller, by roughly 200 Pg (1 Pg = 10^{15} g) and 500 Pg, respectively, than those during preindustrial times (*1*, *2*). On glacial-interglacial time scales, carbon lost from these sources during ice ages must have been stored in the deep ocean (*3*), the largest reservoir of the ocean-land-atmosphere system. Transfer of this substantial amount of carbon back to the atmosphere and land during deglacial periods would inevitably cause perturbations of the deep-ocean carbonate system, including deep-ocean $[CO_3^{2-}]$ and $\delta^{13}C$. Therefore, deep-ocean $[CO_3^{2-}]$ and $\delta^{13}C$ records should provide insights into carbon reorganizations among different reservoirs of the ocean-land-atmosphere system.

Efforts have been made to reconstruct past $[CO_3^{2-}]$ of the ocean's interior using various proxies (*4*–*8*). Each of these approaches has complications specific to the assumptions underlying its methodology. Existing reconstructions are mostly qualitative and limited to low resolutions or Holocene-LGM time slices for restricted regions and, as a consequence, results are still in dispute (*9*). Extensive core-top calibration (*9*) shows that benthic foraminiferal boron/calcium (B/Ca) ratios serve as a quantitative proxy for deep-ocean $[CO_3^{2-}]$ reconstructions. Although the mechanism for the benthic B/Ca relationship with deep-water $[CO_3^{2-}]$ is not yet well understood, subsequent down-core studies (*10*, *11*) strongly support the core-top empirical calibration. Here, we present benthic foraminiferal B/Ca-derived deep-sea $[CO_3^{2-}]$ records for five cores from the three major oceans that are capable of resolving millennial time-scale changes during the past 50,000 years (Fig. 1 and fig. S1). We measured B/Ca in epifaunal benthic foraminifera *Cibicidoides wuellerstorfi*. B/Ca ratios were converted to seawater $[CO_3^{2-}]$ based on the 1.14 μmol/mol per μmol/kg sensitivity obtained from a global core-top calibration (*9*). Replicates of a consistency standard and samples show an average uncertainty (1 SD) of ±4 μmol/mol in B/Ca, corresponding to an error of ±3.5 μmol/kg in seawater $[CO_3^{2-}]$. Detailed information for materials and methods is described in the supporting online material (SOM) (*12*).

In the Caribbean Basin, glacial deep-water $[CO_3^{2-}]$ in site VM28-122 (*10*) was 27 to 34 μmol/kg higher than that during the late Holocene (Table 1 and Fig. 1A). The decreased glacial weight percent of calcium carbonate (%$CaCO_3$) (Fig. 1A) in this core is thus not caused by intensified dissolution but is due to other reasons, such as dilution by terrestrial detritus. By contrast, deep-ocean $[CO_3^{2-}]$ in site BOFS 8K (*11*) located at 4-km water depth in the polar North Atlantic exhibits an opposite pattern, displaying low values during the last glacial period and high values during the Holocene, reminiscent of the typical Atlantic-type %$CaCO_3$ variation (Fig. 1B) (*13*). Glacial-interglacial changes are relatively small in deep-water $[CO_3^{2-}]$ for Indo-Pacific records (Fig.

[1]Lamont-Doherty Earth Observatory of Columbia University, 61 Route 9W/Post Office Box 1000, Palisades, NY 10964–8000, USA. [2]The Godwin Laboratory for Palaeoclimate Research, Department of Earth Sciences, University of Cambridge, Downing Street, Cambridge CB2 3EQ, UK. [3]State Key Laboratory of Loess and Quaternary Geology, Institute of Earth Environment, Chinese Academy of Sciences, Xi'an, 710075, China.

*To whom correspondence should be addressed. E-mail: jiminyu@ldeo.columbia.edu